

## Effect of Insulating Layers in Loop Applicators for Cardiac Cryoablation

Michael Handler\*, Gerald Fischer\*, Michael Seger\*, Roland Kienast\*, Adrian Schuette<sup>†</sup> and Christian Baumgartner\*

\*Institute of Electrical, Electronic and Bioengineering

University for Health Sciences, Medical Informatics and Technology

Eduard Wallnöfer-Zentrum 1, 6060 Hall in Tirol, Austria

Email: {michael.handler|gerald.fischer|michael.seger|roland.kienast|christian.baumgartner}@umit.at

<sup>†</sup>Fraunhofer-Institute for Production Technology IPT

Steinbachstraße 17, 52074 Aachen, Germany

Email: adrian.schuette@ipt.fraunhofer.de

**Abstract**—Cryoablation for the treatment of cardiac arrhythmias inactivates the electrical conduction of arrhythmogenic tissue by freezing. This method has major advantages but also disadvantages compared to radiofrequency ablation. Modeling and simulation of the cryoablation process can be used to reduce the intervention duration and optimize the cryoablation result. In this work, different variants of cryo loops are modeled and simulated using the Finite Element Method. As the wall of the applicator tube has the same thickness in all dimensions the ablation efficiency in tissue direction is reduced by the heating flux of the streaming blood surrounding the applicator. The effects of different insulation layers in blood direction are compared by using heat flux estimations on stationary temperature distributions. As the applicator tube and the insulation layers consist of different fiber materials, anisotropic thermal conductivity is considered in the models. The estimation of thermal longitudinal and transversal conductivity values by a material modeling approach is presented in detail. It is concluded that insulation layers can have positive and unexpected negative effects depending on the insulation position.

**Keywords**—cryoablation; loop applicator; finite element method; heat flux; anisotropic thermal conductivity

### I. INTRODUCTION

Ablation as treatment for cardiac arrhythmias has been established as a method of choice whenever medical treatment fails or cannot be applied [1]. In this minimally invasive procedure, an applicator is inserted via a sheath through either the femoral artery or vein, or through the subclavian artery into the right or left heart's chambers (atria or ventricles) with X-ray guidance. The aim of ablation techniques in the treatment of cardiac arrhythmias is the electrical inactivation of the arrhythmogenic tissue either by heating (radiofrequency ablation) or freezing (cryoablation).

Radiofrequency (RF) ablation has become the gold standard of the catheter-based approach to tachyarrhythmia ablation [2]. In the late 1990s, catheter-based cryoablation became available as alternative to RF ablation [3]. Cryoablation enables the creation of an elongated lesion in one single ablation (freeze) cycle by using a loop applicator. An additional advantage is the application of *ice mapping*. This technique enables the cardiologist to temporarily inactivate

the electrical conduction of small areas of cardiac tissue to test ablation scenarios by cooling to mild temperatures. Another advantage of cryoablation is that it leads to less endothelial disruption than RF ablation [3].

Disadvantages of cryoablation are (i) a higher recurrence rate [4] due to the possible reactivation of the electrical conductivity, and (ii) a longer intervention duration compared to RF ablation [1].

To improve the efficiency of cryoablation and thus reducing the previously mentioned disadvantages, modeling and simulation of the cryoablation process contributes a better understanding of the freezing effects. Seger et al. [1] published a model to simulate the effects of cryoablation mimicking the geometry of a loop shaped cryo-applicator as shown in Figure 1. Such a loop shape applicator enables the creation of a circumferential elongated lesion (approx. 7 cm length) around vessel structure. It can be applied in pulmonary vein ablation for the treatment of atrial fibrillation.

Only a part of the cooling power delivered by the refrigerant is withdrawn from the target tissue. A significant part of the cooling power will create a therapeutically irrelevant heat flow from the circulating blood stream to the cryo-applicator (Figure 1c). Thus, heat exchange between the refrigerant and the blood is considered an undesired loss of cooling power. The spatial limitations imposed by human anatomy onto the construction of catheters also limit the amount of refrigerant which can be used. Efficient use of the refrigerant is therefore crucial. The major scope of this simulation study is to investigate the effect of insulation layers assembled onto elongated cryo-applicators built from fiber reinforced polymers.

In this work, three applicator variants are presented (without insulation, inner insulation, outer insulation). The cooling flux profiles of these variants are compared with each other by creating two dimensional models of the applicators' cross sections. These cooling fluxes are estimated using stationary temperature distributions calculated by the *Finite Element Method (FEM)*.

For realizing mechanically stable loop applicators the material of the applicators consists of carbon fibers embedded

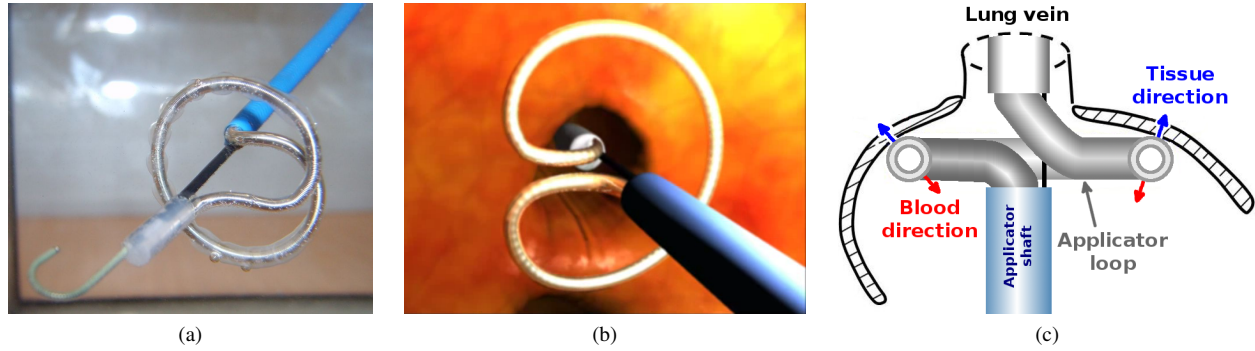


Figure 1. Loop applicator.

(a) Photo of active loop applicator in water (ablation loop partially surrounded by ice).

(b) Position of loop applicator inside the left atrium during cryoablation.

(c) Schematic illustration of applicator loop in left atrium with cross sectional cutthrough demonstrating tissue direction (blue) and blood direction (red) used in the models of Figure 5.

in a silicone matrix. These carbon fibers are spirally wound to form the applicators tube. The insulation layers consist of quartz fibers surrounded by a silicone matrix to withstand mechanical stress. The different thermal conductivities of these materials need to be considered in order to create a representative temperature distribution within the applicator. Therefore, the anisotropic conductivity parameters, longitudinal and transversal thermal conductivity, are estimated in this work for these fiber materials and considered with regard to the fiber orientation in the applicator variants.

In Section II, the mathematical background for the computation of the stationary temperature distribution and anisotropic conductivity parameters is explained and the estimation of the thermal flux to allow comparison of applicator variants is derived. Section III compares the thermal flux properties of the applicator variants, which are discussed in Section IV.

## II. METHODS

In this section, the heat diffusion equation used for the computation of the stationary temperature distributions is described. Subsequently the computation of the parameters of the anisotropic thermal conductivity is explained in detail.

### A. Simulation of Stationary Temperature Distribution

For the models presented in this work, the general heat diffusion equation (1)

$$-\nabla \cdot k(\mathbf{r})\nabla[T(\mathbf{r})] = Q_r(\mathbf{r}), \quad \mathbf{r} \in \Omega \quad (1)$$

has been used to simulate the stationary temperature distributions [5].

The space dependent parameter  $k$  [ $Wm^{-1}K^{-1}$ ] represents the thermal conductivity;  $\mathbf{r}$  holds the cartesian coordinates  $x$  and  $y$  [ $m$ ] in two dimensional models;  $T$  is the unknown stationary temperature [ $K$ ];  $Q_r$  defines the power contribution of distributed volumetric heat sources due to externally applied spatial heating/cooling [ $Wm^{-3}$ ]; and  $\Omega$

denotes the analyzed spatial domain.  $Q_r$  is set to 0 in the current models as the heating/cooling of tissue is integrated into the model by following two types of boundary conditions: *Dirichlet boundary conditions* define known temperatures at the related boundaries. *Cauchy boundary conditions* were used to model the thermal flux of blood/tissue (heating) and the refrigerant (cooling). The thermal flux induced by Cauchy boundary conditions is defined as [1]

$$\frac{\partial \dot{Q}(\mathbf{r})}{\partial \mathbf{n}_\Gamma(\mathbf{r})} = \alpha(\mathbf{r}) \cdot [T(\mathbf{r}) - T_c(\mathbf{r})]; \quad \mathbf{r} \in \Gamma \quad (2)$$

and depends on the difference between the boundary surface temperature  $T$  and the external Temperature  $T_c$ .  $\dot{Q}$  is the heat power [ $W$ ],  $\alpha$  the heat transition coefficient [ $Wm^{-2}K^{-1}$ ],  $\Gamma$  the boundary line and  $\mathbf{n}_\Gamma$  the outward normal to  $\Gamma$ . Additionally, *homogenous Neumann boundary conditions* were used at the symmetry boundaries of the models.

For the numerical computation the analyzed spatial domain is discretized, boundary conditions are applied and the model is solved using the *Finite Element Method (FEM)*. Simulations for cryoablations using loop applicators have been performed similarly by [1]. In a first approximation, the creation of an elongated lesion can be modeled by an essentially cylindrical geometry. Thus, the cross section of the cryo-applicator tube is a two-dimensional plane, which is considered in this study.

### B. Estimation of Thermal Longitudinal and Transversal Conductivity of Anisotropic Materials

At a macroscopic scale it is not possible to consider each single fiber embedded in the polymeric matrix of the tubing. Thus, we first estimate average material properties along and across the fibers assuming that the essentially parallel fibers are arranged in a regular pattern. The applicator tube modeled in this study consists of *carbon fibers* surrounded by a *silicone matrix* (Figure 2).

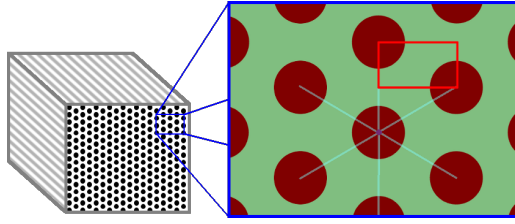


Figure 2. Sketch of the fiber material of the applicator tube. The material consists of equally distributed carbon fibers (red) surrounded by a silicone matrix (green). The red rectangle indicates analyzed domain for the evaluation of thermal transversal conductivity (see Figure 3).

For a proper evaluation of the stationary temperature distribution, the thermal longitudinal and transversal conductivity must be calculated. The average thermal longitudinal conductivity  $\bar{k}_l$  is computed by a weighted average of both the fiber ( $k_f$ ) and the matrix material thermal conductivities ( $k_m$ ) (3):

$$\bar{k}_l = p_f \cdot k_f + (1 - p_f) \cdot k_m \quad (3)$$

$p_f$  defines the volumetric density ( $0 \leq p_f \leq 1$ ) of fiber in the material.

The thermal transversal conductivity was computed by generating a triangular mesh (Figure 3a) of the area within the red rectangle depicted in Figure 2. This area is sufficient for the computation of the thermal transversal conductivity because it represents the repetitive pattern for the cross section of the fiber material. The geometry of the simulated area was determined from the diameter of the carbon fibers ( $7 \mu\text{m}$ ) and the volumetric density of carbon fibers in the material ( $p_f = 0.6$ ).

To generate the model depicted in Figure 3a by using the fiber radius  $r$  and the fiber density in the material  $p_f$  the area covered by fiber  $A_f$  (area of a semicircle) can be calculated by (4)

$$A_f = \frac{r^2 \cdot \pi}{2}. \quad (4)$$

By using the known fiber density of the material, the simulation area  $A_s$  was computed as follows (5):

$$A_s = \frac{A_f}{p_f} \quad (5)$$

The height  $h$  is exactly the half of the diagonal of the model  $d$ . The parameter  $d$  describes the spatial difference between the centers of two neighboring fibers. As depicted in Figure 2 the height  $h$  (see left boundary of red rectangle indicating the simulated area) is exactly half the distance from the centers of the top fiber to the next fiber directly beneath of it. Using the Pythagorean theorem and defining that  $d = 2h$ , the relation between the width  $w$  and height  $h$  can be calculated by (6)

$$w = \sqrt{d^2 - h^2} = \sqrt{4h^2 - h^2} = \sqrt{3}h. \quad (6)$$

The product of width  $w$  and height  $h$  results in the size of the simulation area  $A_s$ . Therefore the width  $w$  can be determined by (7)

$$w = \frac{A_s}{h} = \frac{\sqrt{3}A_s}{w} = \sqrt{\sqrt{3}A_s}. \quad (7)$$

Summarized the width  $w$  and height  $h$  of the model can be calculated by (8)

$$w = \sqrt{\frac{\sqrt{3} \cdot r^2 \cdot \pi}{2 \cdot p_f}}, \quad h = \frac{w}{\sqrt{3}}. \quad (8)$$

Note that the mesh was created by using the software package Altair HyperMesh 10 (Altair Eng. Inc.) and for the visualization of the models AmiraDev 3.0 (TGS Template Graphics Software, Inc.) was used.

Using the result of the stationary temperature distribution of the model as shown in Figure 3b the average thermal transversal conductivity  $\bar{k}_t$  can be estimated. The sum of heating power  $\dot{Q}$  at the bottom of the model is defined as follows:

$$\dot{Q} = \bar{k}_t \cdot \Delta T \cdot \frac{w \cdot l}{h}, \quad \text{and} \quad (9)$$

$$\dot{Q} = -l \cdot \int_{\Gamma_b} k(\mathbf{r}) \cdot \nabla T(\mathbf{r}) \cdot \mathbf{n}_b d\mathbf{r}, \quad \mathbf{r} \in \Gamma_b \quad (10)$$

where  $w$  and  $h$  are the width and height of the simulated area;  $l$  is the length of the fictive model volume in  $z$ -direction;  $\Delta T$  is the temperature difference between the top and the bottom boundary (as Dirichlet boundary conditions were used  $+1^\circ\text{C}$  at the top and  $-1^\circ\text{C}$  at the bottom boundary of the model);  $\Gamma_b$  is the lower boundary of the model;  $\mathbf{n}_b$  is the outward normal at  $\Gamma_b$  ( $\mathbf{n}_b = (0 \ -1)^T$ ). After assigning the thermal properties of Table I the stationary temperature distribution was computed (Figure 3b).

Equation (9) is used to calculate the power  $\dot{Q}$  with known transversal conductivity  $\bar{k}_t$ . This equation was derived from the thermal resistance  $R$  defined by the ratio of temperature difference  $\Delta T$  and the heating power  $\dot{Q}$  at the bottom of the model depicted in Figure 3:

$$R = \frac{\Delta T}{\dot{Q}} \quad (11)$$

Furthermore,  $R$  represents the inverse of the average thermal transversal conductivity  $\bar{k}_t$ . After substituting  $R$  by  $(\bar{k}_t)^{-1}$  and rearranging (11)  $\dot{Q}$  can be expressed by (9). Since the heat power  $\dot{Q}$  is proportional to the width  $w$  and length  $l$  and inversely proportional to the height  $h$  of the model, the factor  $w \cdot l / h$  was added.

As the transversal conductivity  $\bar{k}_t$  is unknown, (10) was used to estimate  $\dot{Q}$  with known stationary temperature distribution [5][6].

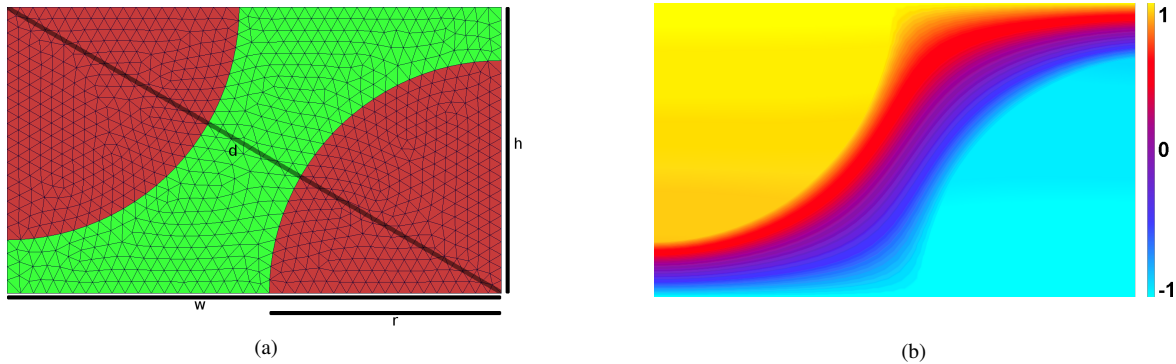


Figure 3. FEM simulation of the selected red rectangular area in Figure 2 to compute the thermal transversal conductivity of the fiber material with carbon fiber density of 60 % and carbon fiber diameter of  $7 \mu\text{m}$ .

(a) Meshed model (red: carbon fiber, green: silicone matrix)

(b) Stationary temperature distribution after applying constant temperatures of  $+1^\circ\text{C}$  at the top boundary and  $-1^\circ\text{C}$  at the bottom boundary of the model

From (9) and (10) we obtain

$$\bar{k}_t = -\frac{h}{w} \cdot \frac{1}{\Delta T} \cdot \int_{\Gamma_b} k(\mathbf{r}) \nabla T(\mathbf{r}) \cdot \mathbf{n}_b d\mathbf{r}; \quad \mathbf{r} \in \Gamma. \quad (12)$$

For the insulating layers, a quartz fiber material was used. Computation of  $\bar{k}_l$  and  $\bar{k}_t$  for this material is done analogously to the carbon fiber material. The resulting values for  $\bar{k}_l$  and  $\bar{k}_t$  for both materials are listed in Table I.

Table I  
MATERIAL PROPERTIES USED IN SIMULATIONS.  
 $\bar{k}_l$  AND  $\bar{k}_t$  REFLECT THE COMPUTED LONGITUDINAL AND TRANSVERSAL CONDUCTIVITIES BASED ON (3) AND (12).

	Applicator	Insulation
Fiber material	Carbon	Quartz
$p_f$	0.6	0.5
$k_f [Wm^{-1}K^{-1}]$	17	1
Matrix material	Silicone	
$k_m [Wm^{-1}K^{-1}]$	0.17	
$\bar{k}_l [Wm^{-1}K^{-1}]$	10.27	0.59
$\bar{k}_t [Wm^{-1}K^{-1}]$	0.66	0.36

The parameters for the thermal conductivity of carbon and quartz fiber were taken out of the material description provided by the manufacturer of the material. The thermal conductivity of silicone was obtained from [7].

### C. Thermal Flux Computation

We can now consider the cryo-applicator tubing at a macroscopic scale by using the average transversal and longitudinal conductivities computed above.

In this work, applicators with different insulation types in blood direction are compared with each other and with an applicator without insulation. To allow a comparison of

ablation efficiency the *thermal flux* was computed over the applicator surface.

Therefore, models of the applicator variants were created (Figure 5). Due to the symmetry only the right half of two dimensional cuts of the applicator variants were modeled. The diameter of all applicator variants is 2.3 mm; the applicator tube without insulation has a thickness of  $181 \mu\text{m}$  and the maximum insulation thickness for both insulated variants is  $245 \mu\text{m}$ . The spatial domain of the models was discretized to allow the numerical computation of the stationary temperature distributions within the applicator variants during cryoablation.

For computation of the stationary temperature distribution the anisotropic thermal conductivities depicted in Table I were used. The carbon fibers of the applicators are aligned clockwise with a winding angle of  $\beta = 80^\circ$ , whereas the fibers of the insulating material are aligned perpendicular to the cross section (see Figure 4). Therefore, the longitudinal conductivity is not considered in the insulating material as only the transversal conductivity of the insulating material is needed.

Cauchy boundary conditions were assigned to the refrigerant boundary  $\Gamma_i$  ( $\alpha = 3000 Wm^{-2}K^{-1}$ ,  $T_c = -90^\circ\text{C}$ ) and to the blood/tissue boundary  $\Gamma_o$  ( $\alpha = 3000 Wm^{-2}K^{-1}$ ,  $T_c = 36.5^\circ\text{C}$ ) [7].

After computing the stationary temperature distribution of the applicators, the thermal flux into the applicator  $P [Wm^{-2}]$  at the boundary  $\Gamma_o$  can be computed similarly to the Cauchy boundary condition in (2):

$$P(\mathbf{r}) = -\frac{\partial \dot{Q}(\mathbf{r})}{\partial \mathbf{n}_\Gamma(\mathbf{r})} = \alpha(\mathbf{r}) \cdot [T_c(\mathbf{r}) - T(\mathbf{r})], \quad \mathbf{r} \in \Gamma \quad (13)$$

$P$  is obtained from the Cauchy boundary condition. Heat flow from the tissue to the applicator is defined as positive. Therefore the multiplicative factor -1 was added to (13).

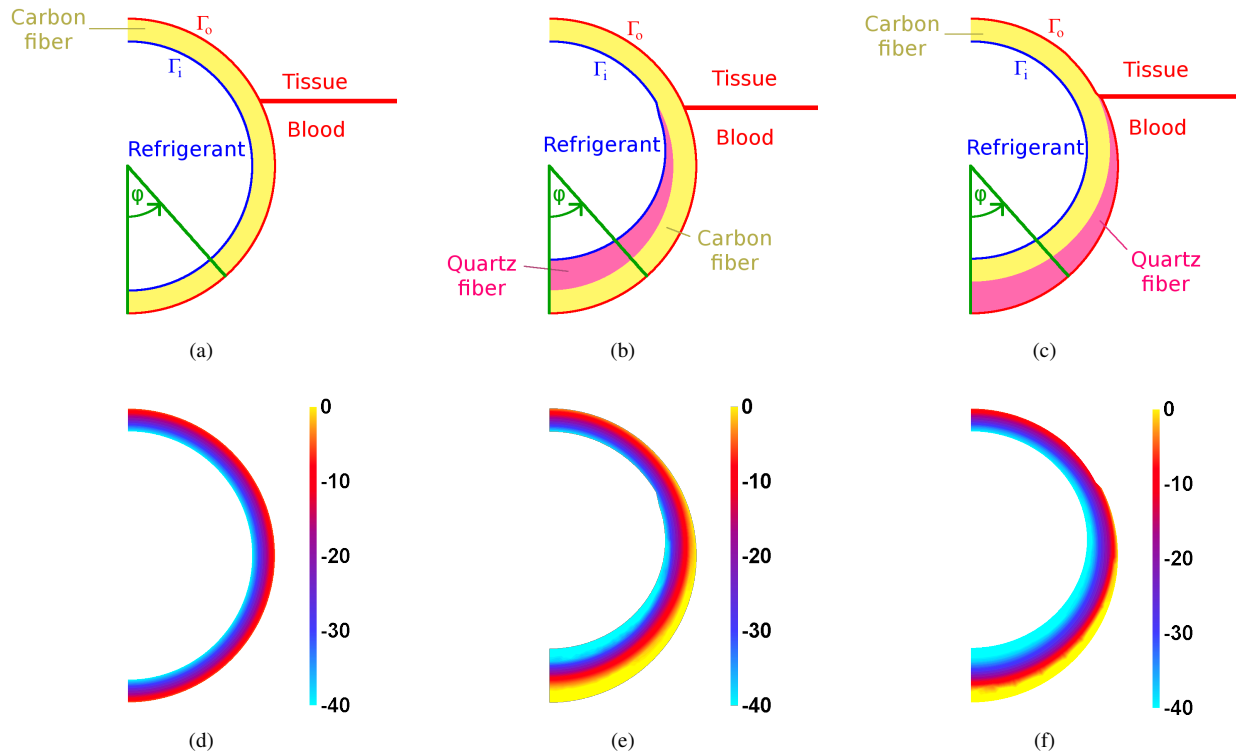


Figure 5. Model of applicator variants. Angle  $\varphi$  is used in Figure 6 for the comparison of the heat flux. (a) without insulation; (b) with inner insulation; (c) with outer insulation; (d) temperature distribution without insulation; (e) temperature distribution with inner insulation; (f) temperature distribution with outer insulation.

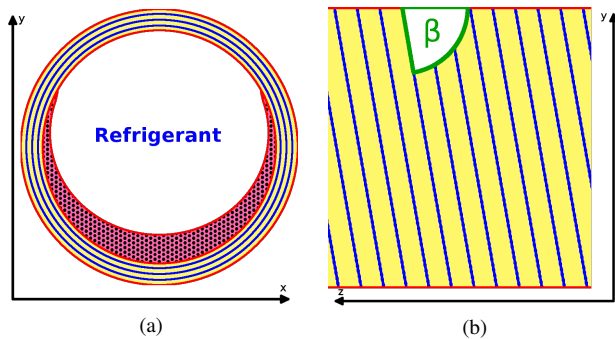


Figure 4. Fiber orientation in applicator models. The fiber orientation of the applicator tube is spirally wound with winding angle  $\beta = 80^\circ$  in  $z$  direction and the fiber orientation of the insulation layer is parallel to the  $z$  axis (winding angle  $0^\circ$ ). (a) Cross section of the applicator variant with inner insulation (blue: carbon fibers of tube; yellow: silicone matrix of carbon fiber material; black: quartz fibers of insulation layer; pink: silicone matrix of insulation layer) (b) Perspective along the applicator surface depicting carbon fibers (blue) spirally wound with winding angle  $\beta = 80^\circ$  in  $z$  direction.

### III. RESULTS

Using the stationary temperature distributions of the models depicted in Figure 5 and the thermal flux equation (13) for the surface  $\Gamma_o$  the angle dependent thermal flux values were computed and compared with each other in Figure 6.

The visualization of the thermal flux starts at the thickest insulation point in blood direction at  $\varphi = 0^\circ$  and proceeds counterclockwise with increasing  $\varphi$  in tissue direction until  $\varphi = 180^\circ$ .

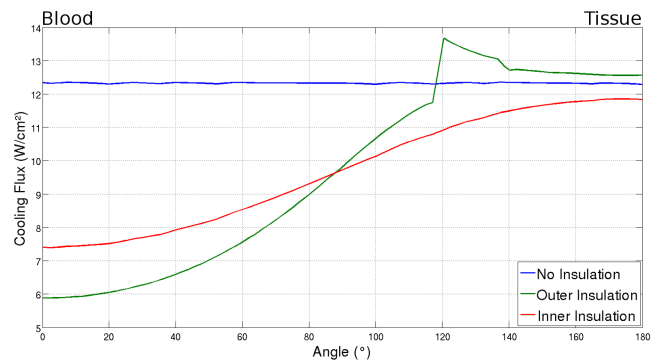


Figure 6. Comparison of angle dependent thermal flux values of the three applicator variants depicted in Figure 5 with  $\varphi = 0^\circ$  at the bottom (blood side) and  $\varphi = 180^\circ$  at the top (tissue side). Angle increases counterclockwise.

As depicted in Figure 6, the thermal flux over the surface of the applicator without insulation has a constant value of  $12.3 \text{ W/cm}^2$ .

The applicator with inner insulation shows a decrease of the cooling flux in blood direction. The minimal thermal flux

of  $7.4 \text{ W/cm}^2$  is present at  $\varphi = 0^\circ$  (maximal thickness of insulation layer). It increases with rising  $\varphi$  and reaches its maximum of  $11.8 \text{ W/cm}^2$  at  $\varphi = 180^\circ$ .

The thermal flux profile of the applicator with outer insulation shows an even lower value of  $5.9 \text{ W/cm}^2$  than both other variants at  $\varphi = 0^\circ$  (maximal thickness of insulation layer). Contrary to the inner insulated applicator the maximum cooling flux is located at  $\varphi = 120^\circ$  with the value of  $13.7 \text{ W/cm}^2$  and reduces with increasing  $\varphi$  until it reaches the value of  $12.6 \text{ W/cm}^2$  at  $\varphi = 180^\circ$ .

#### IV. CONCLUSION AND FUTURE WORK

The major scope of this study is the development of simulation tools, which should guide the development of efficient applicator tubings for the creation of elongated lesions. Three different applicator constructions using fiber reinforced polymers were compared.

As depicted in Figure 6 the best of the three applicator variants presented in this work (without/inner/outer insulation) is the outer insulated applicator. One of the main reasons for the efficiency of this applicator type is the anisotropic thermal conductivity property of the carbon fiber material that directs the cooling power from behind the insulation layer to the tissue front where it is required.

Obviously, the applicator variant without insulation (blue), showed no considerable variations of the thermal flux along the outer boundary. Note that the small variations are caused by spatial discretization and numerical effects.

The applicator variant with inner insulation (red) shows the desired effect of reducing the power loss in blood direction. As a negative side effect the thermal flux in tissue direction is also reduced. This may be caused by the anisotropy of the surrounding carbon fiber material. The inner insulation in blood direction allows for a stronger heating effect of the carbon fiber. Due to the higher thermal conductivity along the carbon fiber the temperature difference between the blood side (warm) and tissue side (cold) is reduced.

The outer insulation of the applicator showed the best results of the applicator variants presented in this investigation. In the direction of blood, a significant cooling flux reduction is seen. Additionally, there is an improved cooling flux in the tissue direction. The maximum at  $\varphi = 120^\circ$  (insulation end for both insulation variants) can be explained by the low temperatures of the carbon fiber material within the insulating layer and the low thermal conductivity of the insulation layer from  $\varphi = 0^\circ$  to  $\varphi = 120^\circ$ . After the insulation layer vanishes at  $\varphi = 120^\circ$  the thermal conductivity rises immediately. At the end of the insulating layer the highest temperature gradient occurs that reduces progressively until  $\varphi = 180^\circ$ .

The manufacturing of an applicator with an additional layer on the outside that does not surround the whole surface may cause mechanical instability of the applicator. Due to

the missing linkage between the two layers it would be necessary to add additional material around the applicator to adhere the insulation to the applicator. Although this provides a possible solution to the problem, this method might reduce the cooling effect of the applicator in tissue direction.

Comparison was carried out by computing a stationary temperature field in a two-dimensional geometry. Such a model seems to be justified for making principle decisions (insulation inside or outside) when starting the development of a production process. Fiber reinforced polymers have been successfully applied in other fields of medical devices such as MR compatible materials [8] and have the potential to increase the efficiency of cryoablation in the future. The results obtained in this study are based on the assumption of an ideal production process, which delivers optimal contact of fibers and polymeric matrix material. In future studies the results should be validated by comparing the simulated predictions with manufactured tubings.

#### ACKNOWLEDGMENT

This work was supported by the K-Regio-Project of the Standortagentur Tirol, Innsbruck, Austria.

#### REFERENCES

- [1] M. Seger, G. Fischer, M. Handler, F. Hintringer, and C. Baumgartner, "Simulating the Spatio-Temporal Spread of Cooling Flux in Cardiac Tissue due to Catheterized Cryoablation," in *Proc. 8th IASTED Int. Conf. on Biomedical Engineering*, ACTA Press, 2011, pp. 83–88.
- [2] D. Lustgarten, D. Keane, and J. Ruskin, "Cryothermal Ablation: Mechanism of Tissue Injury and Current Experience in the Treatment of Tachyarrhythmias," *Progress in Cardiovascular Diseases*, vol. 41, no. 6, pp. 481–498, 1999.
- [3] A. Skanes, G. Klein, A. Krahn, and R. Yee, "Cryoablation: Potentials and Pitfalls," *J Cardiovasc Electrophysiol*, vol. 15, no. 10 Suppl, pp. S28–S34, 2004.
- [4] B. Schwagten, Y. Van Belle, and L. Jordaens, "Cryoablation: how to improve results in atrioventricular nodal reentrant tachycardia ablation?" *Europace*, vol. 12, no. 11, p. 1522, 2010.
- [5] J. Lienhard and J. Lienhard, *A Heat Transfer Textbook*, 4th ed. Phlogiston Press, 2011.
- [6] M. Delfour, G. Payre, and J. Zolesio, "Optimal Design of a Minimum Weight Thermal Diffuser with Constraint on the Output Thermal Power Flux," *Applied Mathematics & Optimization*, vol. 9, no. 1, pp. 225–262, 1982.
- [7] H. Kuchling, *Taschenbuch der Physik*. Hanser Verlag, 2007.
- [8] A. Schuette, C. Brecher, S. Krüger, and G. Krombach, "New Materials for Magnetic Resonance Imaging (MRI) – Fiber-Reinforced Guide Wires and Catheters for Minimal Invasive Interventions," in *World Congress on Medical Physics and Biomedical Engineering, September 7-12, 2009, Munich, Germany*. Springer, 2009, pp. 163–165.